

# Radial and orbital excitations of static-light mesons

Justin Foley,<sup>1</sup> Alan Ó Cais,<sup>2,\*</sup> Mike Peardon,<sup>2</sup> and Sinéad M. Ryan<sup>2</sup>

<sup>1</sup>*Department of Physics, Swansea University, Singleton Park, Swansea SA2 8PP, UK*

<sup>2</sup>*School of Mathematics, Trinity College, Dublin 2, Ireland*

(Dated: October 29, 2018)

We present results for the spectrum of static-light mesons from  $N_f = 2$  lattice QCD. These results were obtained using all-to-all light quark propagators on an anisotropic lattice, yielding an improved signal resolution when compared to more conventional lattice techniques. With a light quark mass close to the strange quark, we have measured the splittings between the ground-state S-wave static-light meson and higher excitations. We attempt to identify the quantum numbers of the excited states in the context of the reduced spatial symmetries of the lattice.

## I. INTRODUCTION

The physics of heavy-light hadrons plays a crucial role in the determination of CKM matrix elements to test the Standard Model and search for new physics. In particular, systems with one or more bottom quarks are of greatest interest but are also the most theoretically and technically challenging. Recently, experiments have begun to probe the excited state spectrum of  $B$  mesons and signals for a number of new states have been seen. It is still unclear if these new states have the expected masses and energies or if they are completely new states, not predicted by the standard theory.

Lattice QCD, in principle, offers the possibility of *ab initio* calculations of the relevant hadronic parameters. However, mass-dependent errors which arise in the discretisation of the Dirac operator have limited the accuracy of heavy-light simulations. Effective theories, which can be used to control or eliminate these errors have been developed and widely used in numerical simulations to predict the masses and decay form factors of stable ground states to better than 10% precision [1]. The static quark approximation is the starting point for one such approach. It is based on the observation that to a good approximation a heavy-light hadron can be described by an idealised system in which the heavy quark is infinitely massive. Heavy-light hadrons exhibit approximate heavy quark spin and flavour symmetries which arise because the Compton wavelength of the heavy quark is much smaller than the typical hadronic length scale ( $m_Q \gg \Lambda_{QCD}$ ). In the static limit these symmetries are exact and the hadron consists of light degrees of freedom bound to a static colour source. Systematic corrections to the static limit can be computed order-by-order in  $\Lambda_{QCD}/m_Q$ , which forms the basis for heavy quark effective theory (HQET). This approach is particularly suitable for hadrons containing a bottom quark where leading order corrections to the static limit, which include chromomagnetic interactions and the heavy quark

kinetic energy, are at the ten-percent level. Although the static approximation is no longer valid for the much lighter charm quark the approach is nevertheless useful. Relativistic simulations at quark masses below charm can be combined with a simulation in the static approximation to allow interpolation to the charm quark mass and in fact this method can also be used to determine  $b$  physics.

Given the utility of the static-quark approximation it may at first appear surprising that this formalism is so under-utilised in lattice simulations. However, simulations in the static quark approximation have suffered from one significant drawback – the signal-to-noise ratio is very poor. Ultimately, this is due to the fact that a static quark propagates only in time. While this makes the static quark propagator trivial to evaluate, in a conventional lattice simulation where one computes only the elements of the light-quark propagator from a single space-time site to all other lattice sites, information on static quark propagation is only obtained from a single spatial lattice site.

Efforts to overcome this problem have focused on two areas. One approach is based on the observation that the signal-to-noise ratio of a static-light two-point function decays exponentially in time with an exponent which receives a large contribution from the static quark self energy. The Alpha collaboration realised that by carefully choosing the discretisation of the static quark action it is possible to reduce the exponent, thereby improving the signal resolution at large times [2].

The second approach, which is used here, is to stochastically estimate the full Dirac propagator [3, 4, 5, 6, 7, 8, 9, 10, 11, 12, 13, 14, 15, 16]. This allows source and sink operators for the static-light correlators to be placed at every spatial lattice site, yielding a dramatic increase in statistics. In this case, it is crucial to optimise the propagator estimate to avoid the introduction of unnecessary noise. In addition to the vast gain in statistics, the use of all-to-all propagators allows for complete freedom in the choice of interpolating operators since the measurement process is decoupled from the evaluation of the propagator. Once the propagator estimate has been computed, one can construct any spatially-extended interpolating field or apply any level of smearing to the quark fields

---

\*Current address: CSSM, School of Chemistry and Physics, University of Adelaide, Adelaide SA5000, Australia

at both the source and sink, without the need for additional fermion matrix inversions. Therefore, an efficient, practical all-to-all algorithm [16] allows us to access not only ground state resonances, but also excited hadronic states.

Of course, the two improvements can be combined and a simulation incorporating both the improved static action and all-to-all propagators may prove to be even more precise. This has not yet been tested.

This paper is concerned with a precision determination of the excited-state spectrum of the  $B_s$  meson. The spectroscopy of the stable ground-state heavy-light meson is already well-studied on the lattice using a variety of approaches including the static approximation [17], the Fermilab [18] approach and NRQCD [19]. However, accurate simulations of the spectrum of radial and orbital excitations, in practice, require an all-to-all propagator algorithm and as a consequence are not as mature.

In this study, we compute the excited-state spectrum of static-light mesons in two-flavour QCD. Experimentally, little is known of the excited-state spectrum of heavy-light hadrons and so predictions from lattice QCD are of considerable phenomenological interest. Simulations of static-light mesons can also be seen as a natural testing ground for all-to-all propagator techniques since they require only a single light propagator per configuration. It is therefore unsurprising that a number of groups have attempted to tackle this particular problem. The static-light excited-state spectrum in dynamical QCD has previously been studied in refs. [20, 21].

In this paper we compute the energies of static-light mesons where the light quark mass is close to the strange quark. Our results are therefore most relevant for the  $B_s$  spectrum. In this case, experimentally, the ground state (pseudoscalar and vector) energies are well established, but there exists no conclusive experimental determination of the excited states [22] [41].

The remainder of the paper is organised as follows. Section II describes the group theory of the static-light spectrum in the continuum and its analogue on the lattice. The construction of lattice operators, their analysis using a variational approach, the all-to-all propagators and lattice actions used are also described. Section III discusses the results of the dynamical simulations including finite volume effects and the spectrum of states. In Section IV we address the issue of multiparticle states. Section V contains a discussion of the results and in Section VI we draw some conclusions.

## II. THE STATIC-LIGHT SPECTRUM

The heavy-quark spin symmetry in the static limit means that mesons which differ only by the spin of the heavy quark are degenerate, ie, there is no hyperfine splitting. In this limit the total angular momentum and parity of the light degrees of freedom ( $J_\ell^{P_\ell}$ ) are conserved quantities, and it is conventional to use these quantum

numbers to label the degenerate hyperfine multiplets [23]. So, for example, the pseudoscalar ( $0^-$ ) and vector ( $1^-$ ) mesons correspond to  $J_\ell^{P_\ell} = \frac{1}{2}^-$ . In the constituent quark model description of hadrons these are S-wave (orbital angular momentum  $L=0$ ) channels. Similarly the P-wave channels have  $J_\ell^{P_\ell} = \frac{1}{2}^+, \frac{3}{2}^+$  and the D waves are  $J_\ell^{P_\ell} = \frac{3}{2}^-, \frac{5}{2}^-$ . Note that we have implicitly assumed that the mesons contain a static quark, which has positive intrinsic parity. In our measurements we exploit the heavy-quark spin symmetry to optimise our signals and average over all degenerate channels. To facilitate this we construct interpolating operators specifically for the light degrees of freedom. We then combine the source and sink operators with a simple Wilson line to obtain a gauge-invariant two-point function with the required quantum numbers [17].

A lattice determination of static-light energies is important in its own right but in addition, such an unambiguous determination of the spectrum can also be used to indicate which quark models most accurately reproduce the static-light physics. Naively, for a given value of  $L$ , one expects a natural ordering of energies to prevail. That is, the multiplet with a larger value of  $J_\ell$  has a higher energy. However, some quark models predict that at higher orbital and radial excitations this ordering should reverse [24, 25]. Whether this reversal in ordering does in fact occur, and at what level it occurs, is still a matter of debate. This phenomenon was first investigated in a dynamical lattice simulation in ref. [26] which concluded that no reversal of ordering occurs up to and including D-wave excitations.

### A. Spatial rotations on the lattice

The accurate determination of the excited-state spectrum requires a precise understanding of lattice space-time symmetries. The angular momentum quantum number  $J$ , assigned to states in the continuum, labels irreducible representations (irreps) of  $SO(3)$ , the group of proper rotations which leaves the continuum QCD Hamiltonian invariant. On a lattice which is isotropic in space, this symmetry group is broken to a 24-element subgroup - the octahedral point group  $O$ .

If we base our analysis solely on the continuum symmetry group then we will almost certainly misidentify some of the excited-state resonances. We therefore compute correlation functions of operators which transform irreducibly under the lattice symmetry group. These operators have non-zero overlap with an infinite number of states, and the continuum quantum numbers of the low-lying states can be deduced by observing (near) degeneracies across the lattice irreps.

The full spatial symmetry group is in fact  $O_h = O \otimes C_2$ , where  $C_2$  consists of the identity and the space inversion operator. The elements of  $C_2$  commute with the group of proper rotations and the irreps of the full symmetry

group follow directly from the irreps of  $O$ . Therefore we first consider the irreps of this subgroup.

The octahedral point group has five conjugacy classes and accordingly five single-valued irreps. These are labeled  $A_1$ ,  $A_2$ ,  $E$ ,  $T_1$  and  $T_2$ , and are of dimension 1,1,2,3 and 3 respectively. Determining the relationship between the angular momentum quantum number and these irreps is relatively straightforward. Restricting the continuum irreps, labeled by  $J$ , to the elements of  $O$  generates representations for  $O$  which are in general reducible. These *subduced* representations can then be decomposed into their constituent irreps.

The number of times a particular irreducible representation of  $O$ , labeled by the superscript  $\alpha$ , occurs in the continuum  $J$  irrep is given by the formula

$$n_J^{(\alpha)} = \frac{1}{N_G} \sum_k n_k \chi_k^{(\alpha)} \chi_k^{(J)}. \quad (1)$$

$N_G$  is the number of group elements, in this case  $N_G = 24$ . The subscript  $k$  labels the conjugacy classes of the lattice symmetry group, and  $n_k$  is the number of group elements in a conjugacy class.  $\chi_k^{(\alpha)}$  is the character of the conjugacy class in the lattice irrep and  $\chi_k^{(J)}$  is the corresponding character in the subduced representation. By applying this formula systematically for a number of values of  $J$ , it is possible to deduce the angular momentum content of the lattice irreps.

The preceding analysis applies to single-valued, or bosonic, representations only. However, interpolating operators for the light fermionic degrees of freedom transform according to the double-valued irreps of  $O$ . To find these, we consider the double-cover group  $O^D$ . This 48-element group has eight irreps, but five of these coincide with the single-valued irreps of  $O$ . The remaining three are labeled  $G_1$ ,  $G_2$  and  $H$ , and these form the double-valued irreps of  $O$ .  $G_1$  and  $G_2$  are both two-dimensional representations, and  $H$  has dimension four. The angular-momentum content of these irreps can be determined using the formula in Eq.(1), where in this case the sum extends over the elements of  $O^D$ , for which  $G_1$ ,  $G_2$  and  $H$  are single-valued representations.

The extension of this discussion to the full spatial symmetry group is clear:  $O_h$  has twice the number of irreps as  $O$ . For example, the irrep  $G_1$  of  $O$  yields the irreps  $G_{1g}$  and  $G_{1u}$  of  $O_h$ . The subscripts  $g$  and  $u$  denote representations which are even (gerade) and odd (ungerade) under spatial inversion, respectively. Table I lists the even-parity irreps of  $O_h$  and the quantum numbers of their low-lying constituent states. The table illustrates an obvious but important point - states which lie in the same continuum irrep, but with different values of  $J_z$  (labeling the rows of the continuum irreps) are in general divided between the lattice irreps. For example, states with quantum numbers  $J_\ell^{P_\ell} = \frac{5}{2}^+$ , corresponding to a 6-dimensional representation of  $O(3)$ , appear in both the  $G_{2g}$  and  $H_g$  irreps. In the continuum, in the absence of an external field, these states are degenerate in energy;

Lattice irrep	Dimension	$J^P$
$G_{1g}$	2	$\frac{1}{2}^+, \frac{7}{2}^+ \dots$
$G_{2g}$	2	$\frac{5}{2}^+, \frac{7}{2}^+ \dots$
$H_g$	4	$\frac{3}{2}^+, \frac{5}{2}^+, \frac{7}{2}^+ \dots$

TABLE I: Even-parity irreducible representations of the octahedral point group with the quantum numbers of the lowest-lying constituent states.

however, this degeneracy is broken by lattice artifacts. Therefore, in a numerical study one hopes to determine the  $\frac{5}{2}^+$  energy levels by identifying near-degenerate levels in the  $G_{2g}$  and  $H_g$  irreps which converge in the approach to the continuum limit.

We are now in a position to assign the states of interest to their respective lattice irreps. We see that the S wave, which has  $J_\ell^{P_\ell} = \frac{1}{2}^-$ , lies in the  $G_{1u}$  irrep. The  $\frac{1}{2}^+$  P wave and the  $\frac{3}{2}^+$  P wave appear in the  $G_{1g}$  and  $H_g$  irreps respectively. The D-wave multiplets are labeled  $\frac{3}{2}^-$  and  $\frac{5}{2}^-$ . Both of these appear in the  $H_u$  irrep, and the  $\frac{5}{2}^-$  states also arise in the  $G_{2u}$  irrep. The lowest-lying states in the remaining lattice irrep, the  $G_{2g}$  representation, are expected to have the quantum numbers  $\frac{5}{2}^+$ , corresponding to F-wave excitations.

## B. Lattice operators

To construct operators which transform according to the irreps of  $O_h$ , we first identify sets of linearly-independent prototype operators which transform amongst themselves under  $O_h$ . The static quark is fixed in space and in this discussion it is convenient to identify the position of the static quark with the origin of a coordinate system. Suitable prototype operators then consist of the spin components of the light quark field which can sit at the origin, yielding local operators, or may be separated from the static quark by a gauge-covariant product of link variables.

The action of  $O_h$  on these prototype operators generates a representation of the group, the operators are said to transform according to the rows of that representation. Interpolating operators which transform according to the constituent irreps can be obtained by taking linear combinations of the prototype operators. A detailed description of how one can construct a complete set of basis operators from a prototype set for the more complicated case of baryon spectroscopy is given in ref. [27]. Here, we simply note that by construction, basis operators for a given instance of a lattice irrep form an orthogonal set.

Before we proceed, it is worth clarifying our terminology. Obviously, by choosing different sets of prototype operators it is possible to construct a number of basis sets for a given irrep, and it may also happen that a particular irrep appears more than once in the decomposition of

one of the prototype representations. For the remainder of the paper, we will say that each disjoint set, transforming according to a particular irreducible representation, corresponds to a single ‘instance’ of that representation.

We work in a spin basis where the upper components of a Dirac spinor have positive parity, while the lower components have negative parity. We can therefore restrict ourselves to prototype operators which use only the upper or lower components of the light quark fields. Operators appearing in a given instance of a representation will only contain either the upper or lower quark field spin components, and we note that exchanging the upper and lower spin components simply changes the parity of the operators.

First we consider local operators. Under  $O_h$  the upper components of the quark field transform according to the  $G_{1g}$  irrep, while the lower components lie in  $G_{1u}$ . All other irreps require spatially-extended operators. The simplest spatially-extended prototype operators consist of light quark field components separated from the static quark by straight-line paths of equal length. For a given path length, 6 offsets need to be considered - displacements along the  $x$ ,  $y$  and  $z$  axes in positive and negative directions. Combining these offsets with two of the four light quark field spin components yields a 12-dimensional representation. This representation decomposes into  $G_{1g}$ ,  $G_{1u}$ ,  $H_g$  and  $H_u$ . All the S, P and D-wave states appear in these irreps. The four irreps can be studied using only local operators and operators with straight-line offsets. However, identification of the D-wave states also requires the use of operators which project onto the  $G_{2u}$  irrep. The simplest such operators can be obtained from a prototype set consisting of spin components displaced from the origin along diagonals in planes spanned by the  $x$ ,  $y$  and  $z$  axes. In terms of link variables these diagonals are given by the sum of two L-shaped paths as shown in Fig. 1. We can consider pro-



FIG. 1: The planar diagonal path connecting the static quark to the light quark field components, which is required to construct operators for  $G_{2u}$ , is given by the sum of two L-shaped paths.

totype operators with more complicated paths to try to identify operators which better overlap with the states of interest. However, for our purposes, operators involving these simplest paths yielded good results. In practice, we do not use ‘bare’ links and quark fields in these interpolating operators. In order to reduce noise in our measurements, the link variables are stout-smearred [28, 29]. In addition, as we describe later, Jacobi smearing [30] of the light-quark fields plays a central role in the determination of the excited-state energies. In both cases the smear-

ing is implemented such that the smeared quark fields and link variables have the same transformation properties under  $O_h$  as their unsmeared counterparts; therefore, the statements made above about the choices of path required to access each irrep are unchanged.

Within this collection of operators, there is still some freedom in the choice of interpolating operators. This is particularly evident in the case of straight-line displaced operators, where the prototype representations using either the upper or lower components have the same decomposition in terms of the lattice irreps. From the operator set, final measurements are performed with the operators which couple optimally to the states of interest. The correlation functions we wish to evaluate give the amplitude for creating a static-light meson, containing a static quark, with the required quantum numbers at some initial time and annihilating the meson at a later time. When we evaluate the amplitude for this process we find that interpolating operators which use the upper components of the light quark field yield noisy measurements. Fortunately, the operators which use the lower quark field components have a larger overlap with the states of interest and give much cleaner signals. To avoid the introduction of unnecessary noise, we restrict ourselves to operators containing the lower quark field components in the evaluation of two-point functions which describe a meson which contains a static quark, propagating forwards in time.

Therefore, the only local operators used transform according to the  $G_{1u}$  irrep, and we use spatially-extended operators to project onto the  $G_{1g}$  representation. As discussed, operators with straight-line paths project onto the  $H_g$  and  $H_u$  irreps, and it is possible to construct operators incorporating planar-diagonal paths which project onto the  $G_{2u}$  irrep. Similar operators can be used to project onto the  $G_{2g}$  irrep. However, the lowest-lying states in this representation are the  $\frac{5}{2}^+$  and  $\frac{7}{2}^+$  F waves. These very heavy states are not of immediate interest to us, and we do not include the  $G_{2g}$  irrep in this study.

Therefore it is possible to evaluate correlation functions for five lattice irreps using only the lower quark field components and the simple gauge-covariant paths listed previously. However, using the transformation property of the fermionic degrees of freedom under time reversal, the upper spin components of the light quark field can be used to further enhance our statistics. So far, the correlation functions have been described in terms of a meson containing a static quark, propagating forwards in time. Formally, the same amplitude can be obtained by reversing the direction of the Wilson line and substituting the upper quark field spin components into the interpolating operators. This is a correlation function for the light degrees of freedom with the same angular momentum, but opposite parity, propagating backwards in time. It can also be regarded as a correlation function for a static-light meson containing a static anti-quark. By averaging over correlators for mesons containing a static quark, and mesons containing a static anti-quark, we ensure that all

four light quark spin components are used in our measurements.

### C. The variational method

The operators described in the previous section couple to all the states appearing in their respective irreps. At sufficiently large times it is expected that the behaviour of the corresponding two-point functions will reduce to the usual single exponential decay with an exponent equal to the energy of the lightest state appearing in that irrep. A variational approach must therefore be applied to compute the energies of higher-lying states in each irrep. To apply the variational method in the lattice irrep  $R$ , we first compute a matrix of correlation functions

$$C_{\alpha\beta}(\tau) \propto \sum_{t,\vec{x}} \langle \Omega | \bar{\mathcal{O}}_{\alpha}^{(R)}(t+\tau, \vec{x}) \mathcal{W}(t+\tau, t; \vec{x}) \mathcal{O}_{\beta}^{(R)}(t, \vec{x}) | \Omega \rangle + \text{T.R.} \quad (2)$$

where the subscripts  $\alpha, \beta$  label interpolating operators for the light degrees of freedom in the irrep  $R$ . The barred operator contains spin components of the fermion field  $\bar{q}(x)$ , which lies in the anti-fundamental representation of colour  $SU(3)$ , and the unbarred operator contains the spin components of  $q(x)$ .  $\mathcal{W}(t+\tau, t; \vec{x})$  is a Wilson line from  $t$  to  $t+\tau$  at the spatial site  $\vec{x}$ . In Eq.(2) only the contribution to the correlator involving the lower quark field components is given explicitly, and the initials T.R. denote the piece involving the upper quark field components, obtained by time reversal. In terms of the interpolating operators appearing in Eq.(2), the operator which optimally couples to the  $n^{\text{th}}$  excited state is given by

$$\phi_n^{(R)}(t, \vec{x}) = \sum_{\alpha} v_{n\alpha} \mathcal{O}_{\alpha}^{(R)}(t, \vec{x}). \quad (3)$$

The real-valued coefficients  $v_{n\alpha}$  form the elements of a vector  $\mathbf{v}_n$  which is obtained by solving the generalised eigenvalue equation

$$C(t_D)\mathbf{v}_n = \lambda_n(t_D, t_0)C(t_0)\mathbf{v}_n, \quad (4)$$

where  $t_0$  is a fixed initial time and  $t_D$  is a later reference time. The eigenvalues in Eq.(4) satisfy  $\lim_{t \rightarrow \infty} \lambda_n(t, t_0) = e^{-E_n(t-t_0)} [1 + \mathcal{O}(e^{-\delta_n(t-t_0)})]$ , where  $E_n$  is the energy of the  $n^{\text{th}}$  excited state and  $\delta_n$  is the absolute value of the energy difference to the nearest state.

The excited state energies can be determined by fitting to optimised correlation matrices

$$\begin{aligned} \tilde{C}_{nm}(\tau) &\propto \sum_{t,\vec{x}} \langle \Omega | \bar{\phi}_n^{(R)}(t+\tau, \vec{x}) \mathcal{W}(t+\tau, t; \vec{x}) \phi_m^{(R)}(t, \vec{x}) | \Omega \rangle \\ &+ \text{T.R.}, \\ &\equiv \mathbf{v}_n C(\tau) \mathbf{v}_m. \end{aligned} \quad (5)$$

To construct the initial correlation matrices,  $C(\tau)$ , we require a set of operators which transform according to the irrep  $R$ . However, these operators cannot lie in a single instance of  $R$  because the correlation between different rows in a single instance of an irrep is zero, rendering the variational method invalid. To obtain correlation matrices we apply a number of levels of Jacobi smearing to the quark field components used in the interpolating operators which generates several instances of the irrep. For each row in  $R$ , cross correlations of operators appearing in different instances of the irrep are computed. This results in a correlation matrix for each row in the irrep. These matrices are identical up to statistical errors and we average over the rows of the irrep to obtain a final correlation matrix. The variational method (Eq.(4), Eq.(5)) is then applied to this averaged correlation matrix to determine the energy of the ground state as well as higher-lying states in  $R$ .

### D. All-to-all propagators

The use of an efficient estimate for all elements of the lattice Dirac propagator lies at heart of this study. Although the move from point-to-all fermion propagators to all-to-all propagators undoubtedly introduces an additional computational overhead into lattice simulations, there exist very many applications in lattice field theory where the benefit of using all-to-all propagators far outweighs this additional cost. The work described here involves two areas where all-to-all techniques are particularly useful. Firstly, the reduction in noise per configuration achieved by averaging the correlation matrices over the lattice volume is essential in studies of static-light systems on rather expensive dynamical background configurations. Secondly, all-to-all propagators are of great advantage in excited state spectroscopy. Because all elements of the lattice propagator are known, the construction of spatially-extended interpolating operators and the smearing of the quark fields require no additional inversions of the fermion matrix. The utility of all-to-all propagators in constructing operators which optimally couple to orbital and radial excitations cannot be overstated.

To estimate all elements of the Dirac propagator we employ the hybrid method introduced in ref. [16]. In this approach, the contribution of the low-lying eigenmodes of the Dirac operator to the fermion propagator is evaluated exactly, since these modes are thought to dominate the long-range physics of interest; the contribution of the higher eigenmodes is then estimated stochastically. In terms of the hermitian fermion matrix  $Q = \gamma_5 M$ , the propagator is simply

$$M^{-1} = Q^{-1} \gamma_5. \quad (6)$$

To proceed,  $Q^{-1}$  is written as a spectral sum which is divided into two pieces

$$Q^{-1} = \bar{Q}_0 + \bar{Q}_1, \quad (7)$$

with

$$\overline{Q}_0 = \sum_{i=1}^{N_{ev}} \frac{1}{\lambda_i} v^{(i)} \otimes v^{(i)\dagger}, \quad \overline{Q}_1 = \sum_{i=N_{ev}+1}^N \frac{1}{\lambda_i} v^{(i)} \otimes v^{(i)\dagger}, \quad (8)$$

where  $Qv^{(i)} = \lambda_i v^{(i)}$  and  $N$  is the rank of the fermion matrix. Therefore, according to our method,  $\overline{Q}_0$ , which contains the first  $N_{ev}$  eigenvectors, is computed exactly.  $\overline{Q}_1$  is the contribution of the higher-lying modes to the propagator, which is estimated stochastically. Using the projection operator,  $P_1 = 1 - \sum_{i=1}^{N_{ev}} v^{(i)} \otimes v^{(i)\dagger}$ , this contribution can be written in a more useful form  $\overline{Q}_1 = Q^{-1}P_1$ .

In a naive stochastic estimate, one generates a set of  $N_r$  random noise sources  $\{\eta_{[1]} \dots \eta_{[N_r]}\}$  with the structure of quark fields and the property that

$$\langle\langle \eta_{[r]}(x) \otimes \eta_{[r]}(y)^\dagger \rangle\rangle \approx \delta_{xy}, \quad (9)$$

where  $x, y$  denote any set of quark field indices and  $\langle\langle \dots \rangle\rangle$  denotes an average over the set of noise vectors. An estimate for  $\overline{Q}_1$  is then given by

$$\overline{Q}_1(x, y) \approx \langle\langle \psi_{[r]}(x) \otimes \eta_{[r]}^\dagger \rangle\rangle, \quad (10)$$

where the set  $\{\psi_{[r]}\}$  is obtained by solving  $\psi_{[r]} = Q^{-1}P_1\eta_{[r]}$  for each source vector. Unfortunately, the variance in this estimate can be quite large, and this error decreases as  $1/\sqrt{N_r}$  so that Eq.(10) becomes exact only in the limit  $N_r \rightarrow \infty$ . However, the stochastic estimate can be improved upon substantially through a careful partitioning or ‘dilution’ of the noise sources. The idea here is to break each original noise source into disjoint pieces according to some set of quark field indices. For example, in time dilution, which appears to play a particularly important role in variance reduction, each noise vector is partitioned as

$$\eta_{[r]}(\vec{x}, t) = \sum_{i=0}^{N_t-1} \eta_{[r]}^{(i)}(\vec{x}, t), \quad (11)$$

where  $\eta^{(i)}(\vec{x}, t) = 0$  for  $i \neq t$ .

One can dilute in any combination of quark field indices, generating  $N_d$  diluted noise vectors from each original source. Inverting the fermion matrix on these diluted sources yields an unbiased estimate for  $\overline{Q}_1$  from a single original noise source

$$\sum_{i=0}^{N_d-1} \psi_{[r]}^{(i)}(\vec{x}, t) \otimes \eta_{[r]}^{(i)\dagger}(\vec{x}_0, t_0). \quad (12)$$

In this study, we use  $Z_4$  noise and each component of the noise sources has modulus 1. For such noise, the limit of full dilution corresponds to an exact evaluation of  $\overline{Q}_1$ . This is in stark contrast to the naive estimate where an infinite number of matrix inversions is required to evaluate the propagator exactly.

Averaging each diluted estimate over the distribution of noise sources means that a total of  $N_{inv} = N_d \times N_r$

matrix inversions are used in the estimator of  $\overline{Q}_1$ . There is considerable freedom in how we partition the noise vectors and the optimal dilution path is that dilution which yields satisfactory results while minimising  $N_{inv}$ .

Although the number of eigenvectors, the number of source vectors and the dilution level required depend very sensitively on the details of the measurement, in our studies of static-light systems we have found that computing the contribution of a small number of the low-lying eigenmodes exactly, and using just one or two noise sources with a moderate level of dilution yields excellent results. The precise details of the fermion propagator estimates used in this study are given in Section II F.

## E. Lattice actions

The lattice gauge and Dirac actions used in this study are described in detail in refs. [31, 32]. They are formulated specifically for anisotropic lattices. The gauge action is Symanzik and tadpole improved with leading discretisation errors of  $\mathcal{O}(a_s^4, a_t^2, \alpha_s a_s^2)$ , where  $a_s$  is the lattice spacing in the spatial directions and  $a_t$  is the lattice spacing in the temporal direction. The fermion action is Wilson-like in the temporal direction but the lattice Lagrangian includes an operator of dimension seven to lift the spatial doublers. This action has leading discretisation errors of  $\mathcal{O}(a_s^3, a_t, \alpha_s a_s)$ . In addition, the spatial links appearing in the fermion action are stout-smearred to reduce radiative corrections.

The anisotropic lattice breaks hypercubic symmetry and introduces two new parameters: the bare quark and gluon anisotropies, denoted  $\xi_q^0$  and  $\xi_g^0$ , which must be tuned so that the measured anisotropy  $\xi = a_s/a_t$  takes a target value, which must be independent of the physical probe used to perform the measurement. In dynamical QCD the tuning procedure is quite complicated but is now well-understood and is described in ref. [33].

The static quark is simulated with the Eichten-Hill action [17] and the static quark propagator is then the product of unsmearred temporal links.

## F. Simulation details

The study was performed at a single lattice spacing with  $N_f = 2$ . Some details of the simulation, for both volumes, are in Table II. The lattice spacing is the same on

Volume	$\beta$	$a_t m_q$	$a_s$	$\xi_q^0$	$\xi_g^0$	Configs
$8^3 \times 80$	1.508	-0.057	$\sim 0.17\text{fm}$	7.43	8.42	232
$12^3 \times 80$	1.508	-0.057	$\sim 0.17\text{fm}$	7.43	8.42	245

TABLE II: A table of simulation parameters for the two volumes used in this study.

both volumes and the light and sea quarks are degenerate

in the simulation. The determination of the bare quark anisotropy,  $\xi_q^0 = 7.43$  and the bare gluon anisotropy,  $\xi_g^0 = 8.42$  is described in ref. [33]. These values were chosen to obtain a physical anisotropy  $\xi = 6$ . Measurements of the anisotropy from the light pseudoscalar dispersion relation on the small and large volumes yield values of 5.94(6) and 5.82(5) respectively, which are consistent with the analysis of ref. [33]. For this parameter set, the ratio  $m_\pi/m_\rho = 0.54$ . Our study is therefore most applicable to the spectrum of  $B_s$  mesons. The temporal lattice spacing, determined from the spin-averaged 1P-1S splitting in charmonium, on the same ensemble [34], was found to be  $a_{1P-1S}^{-1} = 7.04(3)\text{GeV}$ , which implies a value for the spatial lattice spacing,  $a_s$  of approximately 0.17 fm. Simulations were performed on  $8^3 \times 80$  and  $12^3 \times 80$  lattices. The use of two spatial volumes allowed us to identify possible finite-size effects and probable multiparticle excitations in our results.

The gauge configurations were generated using the standard Hybrid Monte Carlo (HMC) algorithm. A more detailed description of the particular improvements to the HMC algorithm, specifically for anisotropic lattices is in reference [33]. The generation of the ensemble of 232 gauge configurations on the small lattice required approximately 5000 CPU hours while the 245 configurations on the larger lattice were generated in approximately 15000 CPU hours.

On each volume, we computed the exact contribution of the 50 lowest-lying eigenmodes to the light quark propagator using the ARPACK implementation of the Lanczos algorithm to determine the eigenvectors. The choice  $N_{ev} = 50$  was based on earlier analyses carried out on the small volume. For similar run parameters, it was found that computing the contribution of a few low-lying eigenmodes to the fermion propagator exactly did result in a significant improvement in signal resolution compared to a purely stochastic estimate for the propagator. However, the gain in precision achieved by including more eigenmodes quickly decreases so that, for our purposes, it was not worth considering  $N_{ev}$  greater than 50. To evaluate the contribution of the higher modes to the light fermion propagator on the small volume, time and colour dilution was applied to two independent noise sources. On the larger volume, a single noise source was used, which was also diluted in time and colour indices.

Once the light fermion propagators had been computed, the evaluation of the correlation matrices was relatively straight-forward. Regarding the use of stout-links in the interpolating operators, we found that satisfactory results were obtained with 30 iterations of the smearing algorithm using a weighting factor of  $\rho = 0.025$ . In order to construct correlator matrices, 8 levels of Jacobi smearing were applied to the light quark fields. The quark field after  $j$  applications of the smearing algorithm is given by

$$q^{(j)}(x) = \left(1 + \kappa \sum_{i=1}^3 D_i^2\right)^{n_\kappa} q^{(j-1)}(x), \quad (13)$$

where  $q^{(0)}(x)$  is the original unsmearred quark field. On both lattices,  $\kappa$  was chosen to be 0.1 and  $n_\kappa$  was fixed at 12. For the spatially-extended interpolating operators, we varied the lengths of the gauge-covariant paths, testing offsets which extended over a single lattice spacing and two lattice spacings in a given direction. We found that the single-link operators coupled optimally to the ground states in each lattice irrep and these are the operators which were used in our final measurements.

### III. RESULTS

In Figures 2 to 6 we plot the effective masses, given by

$$m_{\text{effective}}^{(n)} = \ln \left[ \tilde{C}_{nn}(t)/\tilde{C}_{nn}(t+1) \right], \quad (14)$$

for the correlation matrices in each of the five representations considered. These results on the larger ( $12^3 \times 80$ ) lattice show the high quality of the data. Convincing plateaux, with small statistical errors, are seen for as many as five or six states in each irrep. While the physical significance of the higher-lying levels cannot be pinned down without further study the very precise data give us confidence in our determination of the lower-lying energy states.

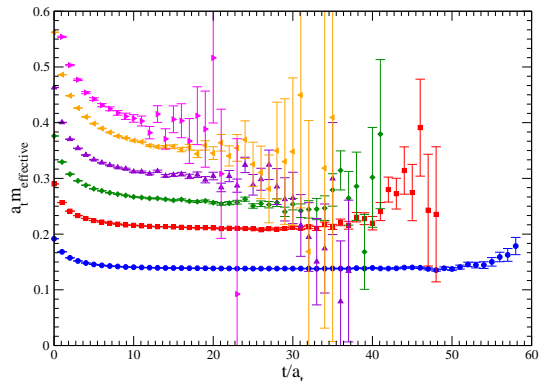


FIG. 2: The effective masses in the  $G_{1u}$  irrep, containing the static-light S wave, determined from the optimised correlation matrix. The ground state and 5 excitations are shown.

#### A. Fitting Procedures

The vectors,  $\mathbf{v}_n$ , used to determine the optimised correlation matrices were obtained by solving the eigenvalue problem in Eq.(4) on time slices  $t_0 = 2$  and  $t_D = 10$ , although we tested other time slices to check for consistency. The resulting correlation matrices are then guaranteed to be diagonal only on time slice 2 and time slice 10. However, for high-quality data we expect the off-diagonal entries of the optimised correlation matrices to be very small over some time interval. In this interval, estimates for the excited state energies can be obtained

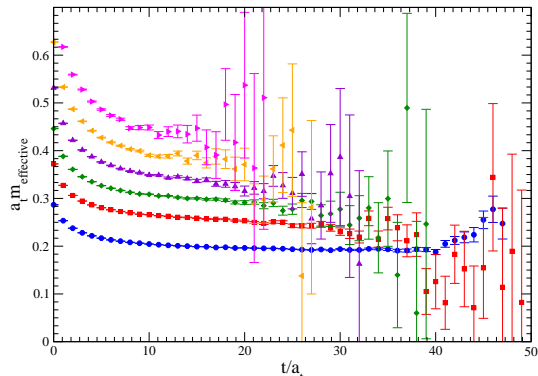


FIG. 3: The effective masses in the  $G_{1g}$  irrep, corresponding to the  $\frac{3}{2}^+ P$  wave. The ground state and 5 excitations are shown.

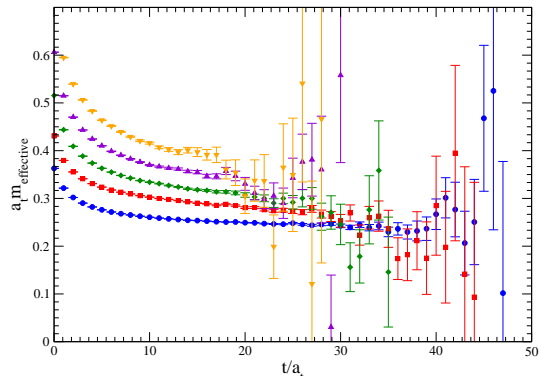


FIG. 5: The effective masses in the  $H_u$  irrep, which contains the  $\frac{3}{2}^-$  and  $\frac{5}{2}^-$  D-wave states. The ground state and four excitations are shown.

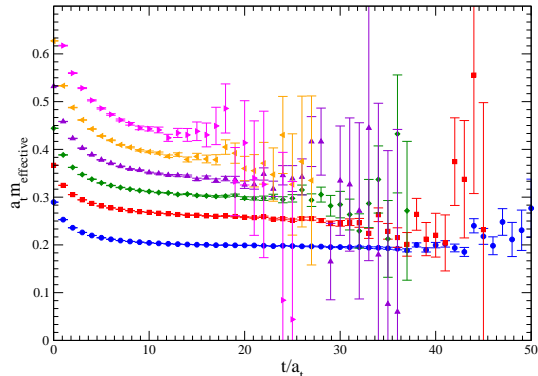


FIG. 4: The effective masses in the  $H_g$  irrep, associated with the  $\frac{3}{2}^+ P$  wave. The ground state and five excitations are shown.

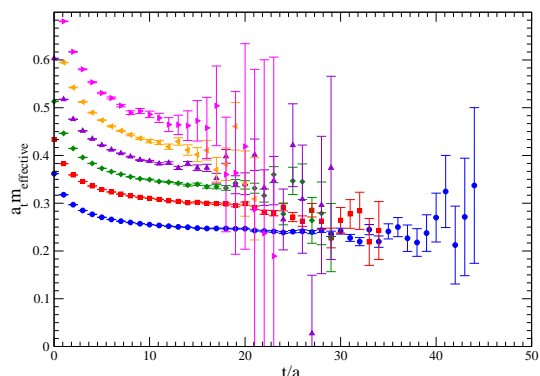


FIG. 6: The effective masses in the  $G_{2u}$  irrep, whose lowest lying state is a D wave. The ground state and five excitations are shown.

by fitting to the diagonal entries in the correlation matrices. The effective masses in Figures 2 to 6, which are defined in terms of the diagonal entries of the correlation matrix, demonstrate that this assumption is reasonable.

However, the most reliable estimates for the low-lying energies are found by including off-diagonal matrix entries in the fit. To implement this, submatrices involving operators which project onto a smaller number,  $M$ , of the lowest-lying states are extracted from the full  $8 \times 8$  optimised matrices. The energies of these states  $E_n$  are determined by fitting to the entries of this submatrix  $\tilde{C}_{PQ}(t)$  using the ansatz

$$\tilde{C}_{PQ}(t) = \sum_{n=0}^{M-1} Z_n^P Z_n^Q e^{-E_n t}. \quad (15)$$

On the small volume, we fit to a  $3 \times 3$  submatrix in the  $G_{1u}$  irrep, and to  $2 \times 2$  matrices in the other irreps. The enhanced signals on the larger volume meant that it was possible to fit to a  $4 \times 4$  matrix in the  $G_{1u}$  irrep and  $3 \times 3$  correlation matrices in the other representations. All the fits use a correlated  $\chi^2$ -minimisation algorithm and statistical errors are determined from 1000 bootstrap

samples.

Since the fitting routine allows for the fact that the operators  $\mathbf{v}_n$  may not be orthogonal, it permits us to fit to time ranges much greater than the optimisation time  $t_D$ . The optimal fit ranges were determined from a sliding window analysis where  $t_{max}$  was fixed at an appropriate value and  $t_{min}$  was varied; the stability of the fitted values and the goodness of fit for varying  $t_{min}$  were then examined. Sample sliding window plots, for the S wave irrep and the  $H_u$  irrep, are shown in Figures 7 and 8. The fitted masses are seen to be consistent over a range of values of  $t_{min}$  with a good  $\chi^2/N_{d.f.}$ . Similar results were found for the five irreps considered. The final fit ranges and the best-fit energies for each of the lattice irreps are given in Table III. In each of these fits, we disregard the result for the highest energy included in the fit since we expect that result to suffer from contamination from higher levels. As an example, for the S-wave ( $G_{1u}$ ) irrep we believe the ground and first two excited states are convincingly determined in our fit procedure. The signal for the remaining higher-lying excitations is still remarkably good, as shown in the effective mass plots and we estimate the energies of these states using single and double



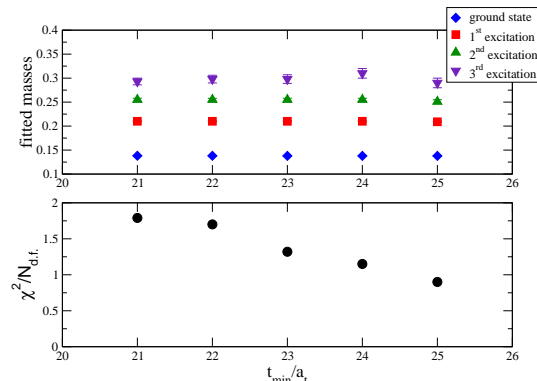


FIG. 7: A sliding window plot for the  $G_{1u}$  irrep. The maximum time slice for these fitted masses is  $t_{\max} = 30$ . The fitted masses in the ground and first three excited states are stable, with good  $\chi^2/N_{\text{d.f.}}$ , when  $t_{\min}$  is varied in fits to the full correlation matrix using four exponentials. Although the range of stable values of  $t_{\min}$  is smaller than seen in Figure 8 the number of states determined is larger.

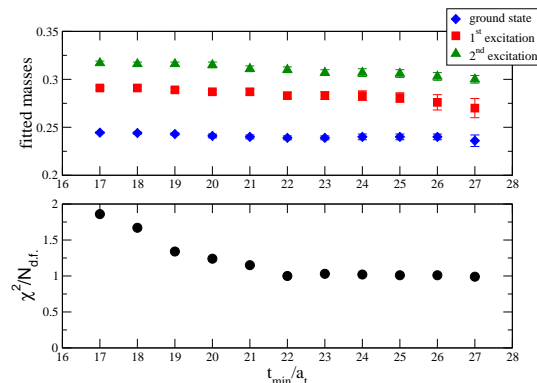


FIG. 8: A sliding window plot for the  $H_u$  irrep. Here  $t_{\max} = 35$  and the ground and first excited states are seen to be stable, with good  $\chi^2/N_{\text{d.f.}}$ , with respect to changes in  $t_{\min}$ .

exponential fits to the relevant correlation matrices,

$$\tilde{C}_{nn}(t) = A_n e^{-E_n t}, \quad (16)$$

$$\tilde{C}_{nn}(t) = A_n e^{-E_n t} (1 + B_n e^{-\Delta_n t}). \quad (17)$$

All the fits were done using a correlated  $\chi^2$ -minimisation algorithm. The statistical errors on the fits were again estimated from 1000 bootstrap samples. Using the double exponential form it was possible to fit to relatively early time ranges, while the single exponential was applicable to later time intervals. We have checked that fitting these ansätze over different time intervals yields consistent results for all the lattice irreps. In addition we have applied this fitting procedure to the lower-lying energies and found that the resulting fitted energies agree within errors with the energies determined using the full correlation matrix, as described above.

We have also compared the effective masses defined in Eq.(14) to effective masses obtained by diagonalising the

Irrep ( $t_{\min}, t_{\max}$ )	Channels			$\chi^2/N_{\text{d.f.}}$
	ground	1 <sup>st</sup>	2 <sup>nd</sup>	
$G_{1u}$ (24,30)	0.1379(2)	0.210(1)	0.255(3)	1.15
$G_{1g}$ (25,30)	0.1906(7)	0.246(4)	0.291(6)	1.37
$H_g$ (25,30)	0.1956(7)	0.257(2)		1.02
$H_u$ (22,35)	0.239(2)	0.283(3)		1.00
$G_{2u}$ (24,30)	0.230(4)	0.283(8)		1.35

TABLE III: The best-fit energies of the ground states and higher excitations of each of the five irreps considered. The energies are given in units of  $a_t^{-1}$ . The fit ranges used and the  $\chi^2/N_{\text{d.f.}}$  values are also given. These results are obtained on the larger of our two volumes,  $12^3 \times 80$ . The errors are statistical only.

correlation matrices on each time slice, as proposed in ref. [35] and found that both approaches agree over the fit intervals.

## B. The spectrum

In the static limit, hadron energies receive an unphysical contribution from the static quark self-energy. However, this contribution cancels in energy differences which are therefore of direct physical significance. The energy differences between the ground state in  $G_{1u}$ , which is the S wave, and higher states are shown in Figure 9. The solid bars are those states determined by a fit to the full correlation matrix. In this case we are satisfied that these numbers correspond to the eigenstates of the lattice Hamiltonian. The dashed boxes denote energy levels obtained by fitting to the diagonal elements of the correlation matrix as described earlier. Although the data indicate that the dominance of the diagonal entries is a reasonable assumption we nevertheless present these results as less conclusive. Table IV lists the splittings shown by the solid bands in Figure 9 in physical units. The lattice spacing has been set from the spin-averaged 1P-1S splitting in charmonium determined on the same configuration set and described in ref. [34].

## C. Finite volume effects

The first indication that finite volume effects might be significant comes from the slight discrepancy between the quark anisotropy on the small and large volumes. The small lattice used in this study has a spatial volume of about  $(1.35 \text{ fm})^3$ . The spatial volume of the large lattice is  $(2.03 \text{ fm})^3$ . Comparing the lowest energy levels in each of the irreps across both volumes, we find small but significant shifts in the energies of the  $G_{1u}$ ,  $G_{1g}$  and  $H_g$  states. The lowest energy levels in the  $H_u$  and  $G_{2u}$  representations remain constant within statistical errors. The  $G_{1u}$  energy level decreases slightly on

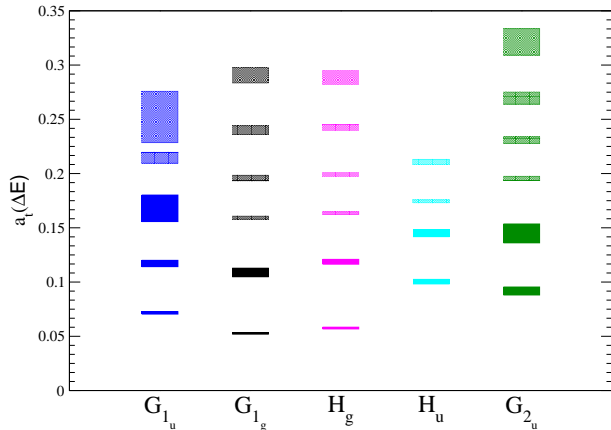


FIG. 9: The splitting between the ground state S wave (ground state in the  $G_{1u}$  irrep) and the other states determined in this study. We show the splitting between states determined from fits to the full correlation matrix as solid bands. Such fits ensure that even small off-diagonal elements of the correlation matrix, which represent leaking between the levels, are taken into account. The shaded bands are those splittings determined, for the higher-lying states, using fits to the diagonal elements of the correlation matrix only. As discussed in the text the data indicate that this is a reasonable procedure, nevertheless we present these states as less conclusively determined. The possible inversion of ordering seen in the D-wave orbital is discussed further in Section V of the text.

channel	$\Delta E$ (GeV)
$G_{1u}$ , 1st excitation	0.504(8)
$G_{1u}$ , 2nd excitation	0.82(2)
$G_{1g}$ , ground state	0.371(6)
$G_{1g}$ , 1st excitation	0.76(3)
$H_g$ , ground state	0.405(6)
$H_g$ , 1st excitation	0.84(2)
$H_u$ , ground state	0.706(2)
$H_u$ , 1st excitation	1.02(2)
$G_{2u}$ , ground state	0.65(3)
$G_{2u}$ , 1st excitation	1.02(6)

TABLE IV: The splitting between the ground state in the  $G_{1u}$  (S-wave) irrep and the other states determined in this analysis by fits to the full optimised correlation matrices. The lattice spacing was determined from the spin-averaged 1P-1S splitting in charmonium, on the same ensemble.

the larger volume. The energies of the  $G_{1g}$  and  $H_g$  states show the strongest volume dependence. The energies of these states increase on the large volume and the splitting between them decreases. This is illustrated in Table V which shows the fitted masses, for the lowest-lying state in each irrep on two volumes. These states are expected to correspond to P wave excitations of the static-light meson. Although a noticeable volume dependence in energies can be a signal for scattering states involving par-

Irrep	Energies	
	$8^3 \times 80$	$12^3 \times 80$
$G_{1u}$	0.1411(5)	0.1379(2)
$G_{1g}$	0.174(1)	0.1906(7)
$H_g$	0.183(2)	0.1956(7)
$H_u$	0.233(3)	0.239(2)
$G_{2u}$	0.224(3)	0.230(4)

TABLE V: A comparison of the fitted energies of the lowest-lying states in each irrep on two volumes. These values are determined in similar fits to the full correlation matrix. The largest effect is seen in the P wave states. The energies of these states increase on the larger volume while the splittings between them decrease.

ticles with non-zero spatial momentum, one expects the energies of such states to decrease on a larger spatial volume. Furthermore, unless the ground state energies in  $H_u$  and  $G_{2u}$  also correspond to multiparticle states, such an assignment is highly unlikely. The possibility that the observed energy levels correspond to two-particle scattering states will be discussed in further detail in Section. IV

#### D. Quark mass and lattice spacing effects

The results presented here have been obtained on gauge configurations generated with a probability density which includes the effects of two degenerate sea quark flavours. The mass of the sea quarks was close to the strange quark mass and the same value was used for the mass of the light valence quark. Therefore, we have simulated a well-defined unitary field theory and our results are free of quenched pathologies. However, we have not explored the inclusion of additional flavours or the use of lighter quark masses. Recent developments in algorithms indicate that these improvements can be implemented with moderate computing resources using the same actions in the near future [36].

The largest uncertainty in our results is due to the fact that we have carried out simulations at just a single lattice spacing. Therefore, although we are confident that the energies we have computed correspond to eigenstates of the lattice Hamiltonian, we are unable to extrapolate these results to the continuum limit. Moreover, the spatial lattice spacing used in the simulations was quite coarse,  $a_s \sim 0.17$  fm, and cutoff effects in our results may be large although we hope that the use of improved actions keeps these errors under control.

## IV. MULTIPARTICLE STATES

It is possible that a number of the energy levels we have computed are not the energies of bound-state resonances but correspond to multiparticle states. The pion mass

measured on this configuration set is  $a_t m_\pi \sim 0.05579$  and one can expect two-particle states consisting of a static-light meson and a pion in particular to contribute to the energy regime shown in Figure 9. Since we have obtained results on two spatial volumes, it should be possible to identify multiparticle resonances by comparing the elements of the optimisation vectors  $\mathbf{v}_n$ , which are computed in the variational method, on both volumes. The normalisation condition for these vectors is  $\mathbf{v}_n^T C(t_0) \mathbf{v}_n = 1$ . A vector projecting onto a bound state is, to a good approximation, volume independent. On the other hand, a vector which isolates a multiparticle state shows a strong, well-defined volume dependence [37]. This dependence comes from the fact that, for example, a state consisting of two weakly-interacting particles in a finite spatial volume has a spectral weight which scales with the inverse volume. The ratio of the volumes used in this study was 3.375, implying that multiparticle excitations should be readily identifiable. However, studies of possible pentaquark candidates have shown that considerable care must be taken when trying to separate single-particle energies from the energies of scattering states on the basis of the volume dependence of spectral weights [38, 39, 40]. In particular, when attempting to isolate the spectral weight of a single state one needs to check for contamination from higher states. We therefore consider the volume dependence of the eigenvectors in conjunction with fit values for the overlap of the optimised interpolating operator onto the state under consideration. We examine the eigenvectors which project onto the three lowest states in the  $G_{1u}$  irrep and the two lowest states in each of the other irreps, for which we have reliable energy measurements. However, we find no evidence for multiparticle contributions to the energy spectrum shown in Fig. 9, although such states undoubtedly exist. We therefore conclude that the interpolating operators used have negligible overlap with low-lying multiparticle resonances. Perhaps this is not so surprising, by construction one expects the interpolating operators to couple strongly to just a few low-lying single-particle states. In fact, given that the operators used in the variational bases differed only in the smearing of the quark fields, it is rather remarkable that the variational method appears to yield good results for so many single-particle resonances.

Ultimately, the issue of multiparticle states in the static-light spectrum will be resolved by using much larger operator bases incorporating interpolating operators specifically chosen to project onto multiparticle states. However, using the data available to us it is possible to make some simple predictions for the multiparticle spectrum. If we assume that the interaction between particles in a scattering state is very weak, we can determine approximate values for the threshold energies for multiparticle states in each of the irreps. For a large enough spatial volume the lowest-energy two-particle states consist of the ground-state S-wave static-light meson and a pion which may have non-zero momentum. We use peri-

odic boundary conditions in the spatial directions so the components of the pion momentum  $\vec{p}$  are quantised in units of  $2\pi/a_s L$ . A pion at rest transforms according to the  $A_{1u}$  irrep of  $O_h$ . However, by applying the elements of  $O_h$  to a pion field with non-zero momentum, one can generate more complicated single-valued representations of the group. Table VI gives the decomposition of pion representations into their constituent irreps for the smallest values of  $|\vec{p}|$  allowed by the lattice. Representations

$\vec{p}$	Irreducible content
(0, 0, 0)	$A_{1u}$
(1, 0, 0)	$A_{1u} \oplus E_u \oplus T_{1g}$
(1, 1, 0)	$A_{1u} \oplus E_u \oplus T_{1g} \oplus T_{2g} \oplus T_{2u}$

TABLE VI: An example of the decomposition of pion representations of  $O_h$ , labeled by the pion momentum in units of  $2\pi/a_s L$ , into their constituent irreps.

for the two-particle scattering states of interest are given by the direct product of the pion representations with  $G_{1u}$ . We then decompose these representations in terms of the double-valued irreps of  $O_h$ . By considering different pion momenta one can deduce the two-particle scattering content of each of the irreps. This procedure is in complete analogy to the determination of the angular momentum content of the irreps described in section II A. The energy of a scattering state is approximated by the sum of the energies of the decoupled states.

$$E_{2P} \approx E_{S.L.} + \sqrt{m_\ell^2 + p^2}, \quad (18)$$

where  $m_\ell$  is the rest mass of the light meson appearing in the scattering state. The threshold for multiparticle states in a particular irrep is the minimum such energy appearing in that representation.

The analysis is complicated by the fact that on the  $12^3 \times 80$  lattice the smallest non-zero momentum component is approximately 0.088, in units of  $a_t^{-1}$ , which lies between the pion and rho masses. Therefore, the lowest-energy scattering state in a given irrep may contain a rho meson at rest rather than a pion with non-zero momentum. Moreover, the unit of momentum is also of the same order of magnitude as the splittings shown in Figure 9, so it is possible that the threshold levels in some irreps correspond to states containing a static-light meson which lies in a representation other than  $G_{1u}$ . We have considered both possibilities and find that on this spatial volume the threshold energies do in fact correspond to two-particle scattering states involving only the S-wave static-light meson and a pion. However, the threshold energy in  $H_g$  is degenerate within errors with the energy of a scattering state consisting of an S-wave static-light meson and a rho meson at rest. The lowest threshold across the irreps is in  $G_{1g}$  and it is associated with a pion at rest. The threshold energies in  $G_{1u}$ ,  $H_g$  and  $H_u$  correspond to a pion with momentum (1, 0, 0) in units of  $2\pi/a_s L$ . In  $G_{2u}$  the lowest allowed pion momentum

is  $(1, 1, 0)$ . In Figure 10 we have inserted the thresholds for multiparticle excitations into the splitting plot previously shown in Figure 9. The dashed red lines indicate

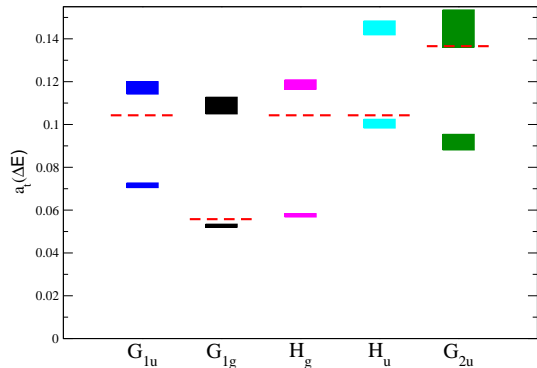


FIG. 10: Splittings between the energy of the ground-state S-wave static-light meson and other low-lying measured energies. The dashed red lines show the scattering thresholds in each of the irreps. The position of the threshold in the  $G_{1g}$  irrep corresponds to the rest mass of the pion. The thresholds in the other irreps correspond to two-particle states containing a pion with non-zero momentum.

the scattering thresholds, and we see that multiparticle states should be detectable in all five irreps over the range of energies investigated in this study.

## V. DISCUSSION

Although a final determination of the excited state spectrum requires simulations at several lattice spacings, it is possible to draw some conclusions from the results obtained here.

First we consider energy levels in  $G_{1u}$ . The lowest-lying state in this irrep is the  $J_\ell^{P_\ell} = \frac{1}{2}^-$  S wave. The next lowest angular momentum value allowed in this irrep is  $J_\ell = \frac{7}{2}$ . The  $\frac{7}{2}^-$  state corresponds to an L=4 or G wave excitation. We expect such a state to be extremely heavy and also to appear as a degenerate level in other lattice irreps. Since this is not the case we therefore conclude that the energy-levels lying directly above the ground state correspond to radial excitations of the  $\frac{1}{2}^-$ . Similarly, the lowest-energy state in the  $G_{1g}$  irrep is the  $\frac{1}{2}^+$ , and we expect the first excited state to be a radial excitation with the same quantum numbers. The interpretation of the higher-lying states is slightly more ambiguous due to the appearance of the  $\frac{7}{2}^+$  F-wave state in this irrep. In the  $H_g$  irrep the ground state has quantum numbers  $J_\ell^{P_\ell} = \frac{3}{2}^+$ . This state lies slightly above the  $\frac{1}{2}^+$  ground state in the  $G_{1g}$  irrep. These are P-wave excitations. The data show solid evidence that the natural ordering prevails in the P-wave sector ( $m_{\frac{3}{2}^+} > m_{\frac{1}{2}^+}$ ). While this splitting is very small it has been measured in this work to be different from zero at the  $5\sigma$  confidence

level. The discussion of natural ordering is made more complicated by the fact that the  $G_{1g}$  ground state lies close to the estimated S wave decay threshold. The first excited state in  $H_g$  lies just above its counterpart in  $G_{1g}$  and we also identify it as a radial excitation with P wave quantum numbers.

To make sense of the energy levels in  $H_u$  one needs to consider them together with the states appearing in  $G_{2u}$ . To begin with, we will assume that the variational analyses have succeeded in determining all the low-lying single particle energies in the  $H_u$  and  $G_{2u}$  irreps, and consider how the relative ordering of D-wave states should effect the simulation results. Recall that both the  $\frac{3}{2}^-$  and  $\frac{5}{2}^-$  appear in the  $H_u$  irrep and only the  $\frac{5}{2}^-$  D-wave contributes to the  $G_{2u}$  irrep. In the standard ordering of states, the  $\frac{3}{2}^-$  is lighter than the  $\frac{5}{2}^-$  which implies that the lowest-lying state in  $H_u$  should lie below the lowest-energy state in the  $G_{2u}$  irrep. One of the higher energy levels in the  $H_u$  irrep, corresponding to the  $\frac{5}{2}^-$  multiplet, should then be degenerate with the lowest energy level in  $G_{2u}$ . This scenario is clearly not supported by the data.

Another possibility is that inversion of the D-wave multiplets does occur. In this case, the ground state energies in  $H_u$  and  $G_{2u}$  are degenerate up to lattice artifacts. The energies of the first excited states in these irreps overlap, and these states may correspond to a radial excitation of the  $\frac{5}{2}^-$ . This would mean that the  $\frac{3}{2}^-$  state is the third level in the  $H_u$  irrep which has no counterpart in the  $G_{2u}$  irrep. However, it seems very unlikely that the splitting between the D-wave multiplets is so large. It could also be the case that systematic errors in the data are particularly severe in these channels, and that at finer lattice spacings and larger volumes the second energy level in  $H_u$  shifts towards the ground state while the third energy level aligns itself with the second level in the  $G_{2u}$  irrep. One could then identify the second level in  $H_u$  with the  $\frac{3}{2}^-$  excitation, and the third level in  $H_u$  and the second state in  $G_{2u}$  would correspond to a radial excitation of the  $\frac{5}{2}^-$ . However, given that the results were obtained using improved actions on a  $(2.03 \text{ fm})^3$  spatial volume, it is improbable that systematic errors could account for such significant shifts in the spectrum.

The inconsistencies between the data and the possible orderings of states seem to suggest that the assumption on which the preceding argument is based is incorrect, and we have not succeeded in measuring all of the lowest-lying single-particle energies in  $H_u$  and  $G_{2u}$ . In particular, there appear to be gaps in the spectrum of the  $H_u$  irrep. This is not surprising when we recall that each variational basis consists of operators which have identical offsets. It appears that a complete determination of the spectrum will require a much greater variety of basis operators with varying degrees of overlap with all the low-lying states. Naively, the fact that the two lowest-lying measured energies in  $H_u$  are close to their counterparts in  $G_{2u}$  might indicate that these are the energies of  $\frac{5}{2}^-$  states. However, we have already noted

that the third level in  $H_u$  does not have a partner in  $G_{2u}$ , and there is no reason why the lower energies in  $H_u$  could not correspond to  $\frac{3}{2}^-$  excitations. Therefore, identification of the lowest measured energy levels in the  $H_u$  irrep requires further investigation.

In spite of the difficulty in interpreting the data, our study of the  $H_u$  and  $G_{2u}$  irreps has been quite successful, and we would like to emphasise two points. Firstly, we have been able to measure the energies of the ground-state  $\frac{5}{2}^-$  D-wave and a radial excitation. These correspond to the first and second energy levels in the  $G_{2u}$  irrep. Secondly, the possibility that the interpolating operators are not coupling to all the low-energy states has only come to light because we have been able to precisely determine a number of energies in each of the irreps which we have compared to theoretical predictions.

Finally, it is worth comparing our data with experimental data for the  $B_s$  spectrum. The energy difference between the  $B_{s,J}^*(5850)$ , with unknown quantum numbers, and the ground-state pseudoscalar  $B_s^0$  is approximately 485 MeV. This number is very close to our value for the splitting between the ground-state S wave and its first radial excitation. However, once  $1/m_Q$  corrections are taken into account, we see that the splitting is also consistent with a P-wave identification for the heavier state.

## VI. CONCLUSIONS

We have presented an *ab initio* study of the spectrum of static-light mesons in  $N_f = 2$  lattice QCD. Previously, computational constraints have made it difficult to determine the excited state spectrum to satisfactory accuracy. We have overcome these constraints using an efficient estimate for all elements of the lattice Dirac propagator. With this method and exploiting translational invariance, we are able to average correlation functions over the whole volume of the lattice, yielding a dramatic reduction in the variance of our Monte Carlo estimates. The use of all-to-all propagators also facilitates the construction of

spatially-extended interpolating operators which project onto the excited states. The construction of these operators and proper interpretation of the final numerical results depend on a clear understanding of the spatial symmetries of the lattice, and our results are given in terms of the irreducible representations of the octahedral point group.

We have succeeded in determining a number of excited state splittings in five of the six double-valued representations. A comparison of results obtained on two different spatial volumes indicates that that our results correspond to the energies of single-particle bound states. We have presented solid evidence (at the  $5\sigma$  level) that the natural ordering of P-wave static-light mesons prevails. We have been able to identify a number of radially excited states however a complete survey of the low-energy spectrum will require further work including, ultimately, an extrapolation to the continuum limit.

A natural progression in this study would include the use of interpolating operators with more complicated offsets which might better couple to heavier single-particle excitations, and the use of operators specifically constructed to couple to multiparticle states. We are also confident that a similar approach to the one used here can shed considerable light on the spectrum of heavy-light baryons.

## Acknowledgments

This work was supported by the IITAC project, funded by the Irish Higher Education Authority under PRTL1 cycle 3 of the National Development Plan and funded, in part, by an IRCSET postgraduate award. We are grateful to the Trinity Centre for High-Performance Computing for their support. We would like to thank Colin Morningstar and Jimmy Juge for kindly allowing us to use their correlator fit code. We also wish to thank Jon-Ivar Skullerud and Buğra Oktay for carefully reading this manuscript.

- 
- [1] T. Onogi, PoS. **LAT2006**, 017 (2006), [hep-lat/0610115].
  - [2] M. Della Morte, A. Shindler and R. Sommer, JHEP **08**, 051 (2005), [hep-lat/0506008].
  - [3] K. Bitar, A. D. Kennedy, R. Horsley, S. Meyer and P. Rossi, Nucl. Phys. **B313**, 348 (1989).
  - [4] Y. Kuramashi, M. Fukugita, H. Mino, M. Okawa and A. Ukawa, Phys. Rev. Lett. **71**, 2387 (1993).
  - [5] S.-J. Dong and K.-F. Liu, Phys. Lett. **B328**, 130 (1994), [hep-lat/9308015].
  - [6] G. M. de Divitiis, R. Frezzotti, M. Masetti and R. Petronzio, Phys. Lett. **B382**, 393 (1996), [hep-lat/9603020].
  - [7] TXL, N. Eicker *et al.*, Phys. Lett. **B389**, 720 (1996), [hep-lat/9608040].
  - [8] UKQCD, C. Michael and J. Peisa, Phys. Rev. **D58**, 034506 (1998), [hep-lat/9802015].
  - [9] UKQCD, C. McNeile and C. Michael, Phys. Rev. **D63**, 114503 (2001), [hep-lat/0010019].
  - [10] W. Wilcox, hep-lat/9911013.
  - [11] H. Neff, N. Eicker, T. Lippert, J. W. Negele and K. Schilling, Phys. Rev. **D64**, 114509 (2001), [hep-lat/0106016].
  - [12] A. Duncan and E. Eichten, Phys. Rev. **D65**, 114502 (2002), [hep-lat/0112028].
  - [13] MILC, T. A. DeGrand and U. M. Heller, Phys. Rev. **D65**, 114501 (2002), [hep-lat/0202001].
  - [14] SESAM, G. S. Bali, H. Neff, T. Duessel, T. Lippert and K. Schilling, Phys. Rev. **D71**, 114513 (2005), [hep-

- lat/0505012].
- [15] M. J. Peardon, Nucl. Phys. Proc. Suppl. **106**, 3 (2002), [hep-lat/0201003].
  - [16] J. Foley *et al.*, Comput. Phys. Commun. **172**, 145 (2005), [hep-lat/0505023].
  - [17] E. Eichten and B. Hill, Phys. Lett. **B240**, 193 (1990).
  - [18] A. X. El-Khadra, A. S. Kronfeld and P. B. Mackenzie, Phys. Rev. **D55**, 3933 (1997), [hep-lat/9604004].
  - [19] W. E. Caswell and G. P. Lepage, Phys. Lett. **B167**, 437 (1986).
  - [20] J. Koponen *et al.*, hep-lat/0702006.
  - [21] T. Burch and C. Hagen, Comput. Phys. Commun. **176**, 137 (2007), [hep-lat/0607029].
  - [22] Particle Data Group, W. M. Yao *et al.*, J. Phys. **G33**, 1 (2006).
  - [23] N. Isgur and M. B. Wise, Phys. Rev. Lett. **66**, 1130 (1991).
  - [24] H. J. Schnitzer, Phys. Lett. **B226**, 171 (1989).
  - [25] N. Isgur, Phys. Rev. **D57**, 4041 (1998).
  - [26] UKQCD, A. M. Green, J. Koponen, C. McNeile, C. Michael and G. Thompson, Phys. Rev. **D69**, 094505 (2004), [hep-lat/0312007].
  - [27] S. Basak *et al.*, Phys. Rev. **D72**, 094506 (2005), [hep-lat/0506029].
  - [28] C. Morningstar and M. J. Peardon, Phys. Rev. **D69**, 054501 (2004), [hep-lat/0311018].
  - [29] S. Basak *et al.*, PoS **LAT2005**, 076 (2006), [hep-lat/0509179].
  - [30] S. Gusken *et al.*, Phys. Lett. **B227**, 266 (1989).
  - [31] TrinLat, J. Foley, A. O’Cais, M. Peardon and S. M. Ryan, Phys. Rev. **D73**, 014514 (2006), [hep-lat/0405030].
  - [32] C. Morningstar and M. J. Peardon, Nucl. Phys. Proc. Suppl. **83**, 887 (2000), [hep-lat/9911003].
  - [33] R. Morrin, A. O’Cais, M. Peardon, S. M. Ryan and J.-I. Skullerud, Phys. Rev. **D74**, 014505 (2006), [hep-lat/0604021].
  - [34] K. J. Juge *et al.*, PoS **LAT2006**, 193 (2006), [hep-lat/0610124].
  - [35] M. Luscher and U. Wolff, Nucl. Phys. **B339**, 222 (1990).
  - [36] L. Del Debbio, L. Giusti, M. Luscher, R. Petronzio and N. Tantalo, JHEP **02**, 011 (2006), [hep-lat/0512021].
  - [37] N. Mathur *et al.*, Phys. Rev. **D70**, 074508 (2004), [hep-ph/0406196].
  - [38] K.-F. Liu and N. Mathur, Int. J. Mod. Phys. **A21**, 851 (2006), [hep-lat/0510036].
  - [39] C. Alexandrou and A. Tsapalis, PoS **LAT2005**, 023 (2006), [hep-lat/0509139].
  - [40] C. Alexandrou and A. Tsapalis, Phys. Rev. **D73**, 014507 (2006), [hep-lat/0503013].
  - [41] The quantum numbers of the  $B_{s,J}^*$ (5850) are as yet unknown.